Correlations and fluctuations in high energy heavy ion collision experiments*

ZHOU Dai-Mei(周代梅)[1)] WANG Ya-Ping(王亚平)[2)] WEI Li-Hua(韦利华) CAI Xu(蔡勖)[3)]

(Institute of Particle Physics, Central China Normal University, Wuhan 430079, China)

Abstract An overview of research status of soft physics in high energy heavy-ion collision experiments and recent experimental results are presented. The experimental status on fluctuations and correlations has been reviewed and the outlook for research status of soft physics in LHC/ALICE has been introduced in this paper.

Key words quark-gluon plasma, soft physics, correlation, fluctuation

PACS 25.75.-q

1 Introduction

This paper presents an overview of soft physics from SPS to RHIC and discusses what new knowledge can be learned from the results on the bulk properties of high energy heavy ion collisions. This overview focuses on fluctuations and correlations. Seven areas will be discussed:

1) Fluctuations of particle multiplicity. The energy dependence of multiplicity fluctuations in high energy heavy ion collisions can be used to look for experimental signature of increased fluctuations due to a phase transition or the critical point and for the predicted reduction of fluctuations in relativistic hadron gas due to conservation low.

2) Fluctuations of particle ratios, which have been considered as a possible signature of quark gluon plasma formation.

3) Transverse momentum p_{t} fluctuations and correlations, which studied very extensively. The study of nuclear matter at large energy density and the possibility of a transformation to color-deconfined or QCD matter have been the central goals. By analogy with the thermodynamics of ordinary matter critical fluctuations have been viewed as a means to demonstrate transitions across the QCD phase boundary. In particular, critical fluctuation of $\langle p_{\mathrm{t}}\rangle$ or event-wise mean p_{t} as an analog to temperature have been sought.

4) Hanbury Brown-Twiss (HBT) correlations, which can be used to explore the space-time evolution and freeze-out of the system.

5) Forward backward multiplicity correlation. The study of correlations among particles produced in different rapidity regions may provide understanding of the mechanism of particle production.

6) Fluctuation of elliptic flow, which is very sensitive to the initial eccentricity fluctuations.

7) Jet-medium interaction, which probes the early-stage of the medium.

The overview of global properties of soft physics, including collision geometry, particle production, hadronization and flow will be presented by WANG Ya-ping, et al.[1, 2]. We also suggest readers refer to an overview that titled "Experimental Status of Ultra-high Energy Induced Nuclear Reactions" presented by CAI Xu and ZHOU Dai-mei[3].

2 Fluctuations and correlations

The study of fluctuation and correlation has special importance while investigating the existence of possible phase transition in relativistic heavy ion collisions. Event by event fluctuations in the thermodynamic quantities provide important insight towards the physical properties of the dense nuclear matter

Received 21 May 2007

* Supported by Ministry of Education of China (306022) and National Natural Science Foundation of China (10635020,10705012)

1) E-mail: zhoudm@phy.ccnu.edu.cn
2) E-mail: wangyp@iopp.ccnu.edu.cn
3) E-mail: xcai@mail.ccnu.edu.cn

produced in the collisions along with the knowledge of nature of quark-hadron phase transition[4]. The enhanced fluctuation of energy density points to the first order phase transition whereas a second order phase transition may result into divergence of specific heat.

Event by event fluctuations might be a useful signature of phase transition evidence, since they could be significantly altered if a phase transition occurs shortly after the collision[5]due to the large difference between the degree of freedom of the two phases. Since fluctuation observables are intrinsically related to particle correlations, the study of fluctuations could also provide helpful insights on the mechanisms of particle production in heavy ion collisions. Fluctuations in particle multiplicity, ratios, transverse momenta, elliptic flow etc. will be displayed in this paper.

2.1 Fluctuations of particle multiplicity

The energy dependence of multiplicity fluctuations was studied for the most central Pb+Pb collisions at 20, 30, 40, 80 and 158 AGeV by the NA49 experiment at the CERN SPS[6]. The basic measure of multiplicity fluctuations used in this analysis is the scaled variance:

$$\omega = \frac{Var(n)}{\langle n \rangle}$$

where $Var(n)$ and $\langle n \rangle$ are the variance and mean of multiplicity distributions, respectively.

The scaled variance for positively ($\omega(h^+)$), negatively ($\omega(h^-)$) and all charged hadrons ($\omega(h^\pm)$) are presented here. The scaled variance of a Poisson distribution is 1, independent of its mean multiplicity. A larger ω might indicate additional non-statistical fluctuations, a smaller ω might be a hint for a suppression of fluctuation e.g. due to conservation laws. Fig. 1 shows the centrality dependence of multiplicity fluctuation in Pb+Pb collisions at different energies for central collisions. In general ω decreases with increasing the centrality, this trend is stronger for higher energies.

Figure 2 shows the energy dependence of multiplicity fluctuations in Pb+Pb collisions. It can be seen that at all energies the scaled variance for positively and negatively charged hadrons is smaller than 1, the value for a Poissonian distribution.

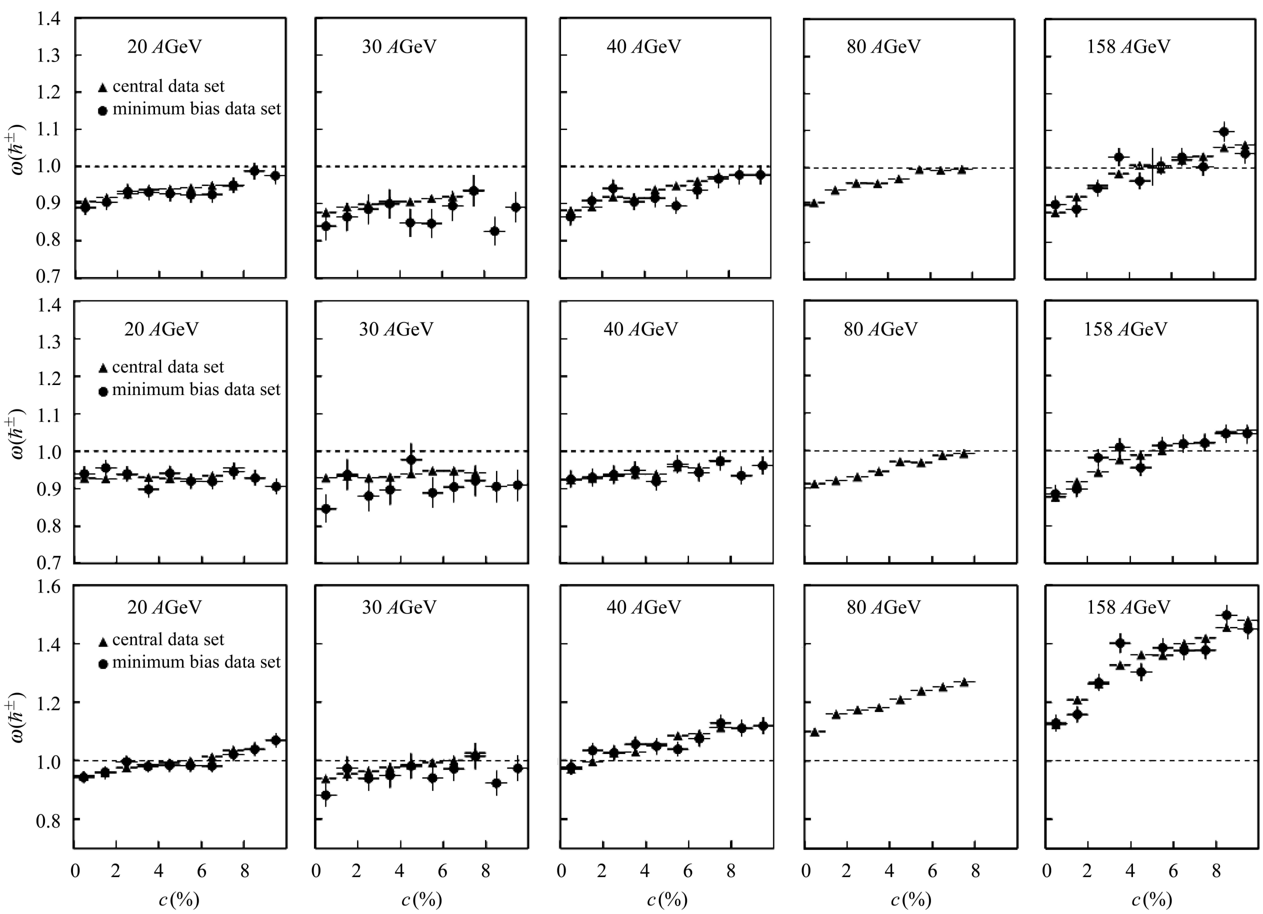

Fig. 1. Centrality dependence of $\omega(h^+)$ (top), $\omega(h^-)$ (middle) and $\omega(h^\pm)$ (bottom) for Pb+Pb collisions at different energies. $C<1\%$ corresponds to the most central collisions. The shown centrality range of $C<10\%$ corresponds approximately to the number of projectile participants $N_{\rm p}^{\rm proj}>160$. Only statistical errors are shown.

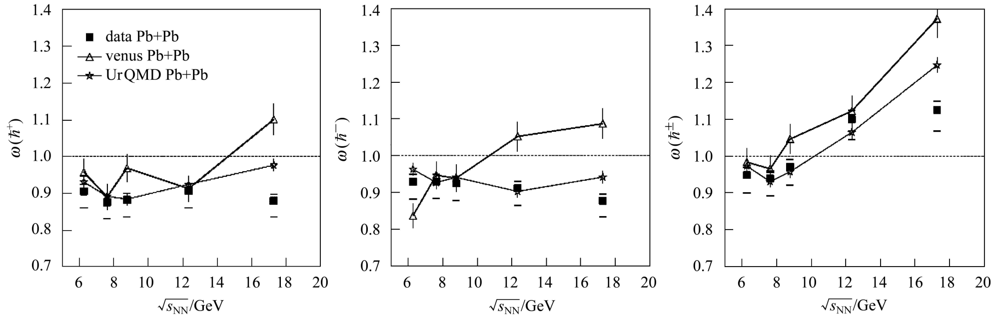

Fig. 2. Energy dependence of multiplicity fluctuations in the most central ($C < 1\%$, Venus calculations: $C < 2\%$) Pb+Pb collisions in comparison with string hadronic model predictions for $\omega(h^+)$ (left), $\omega(h^-)$ (middle) and $\omega(h^\pm)$ (right).

At RHIC energy, PHOBOS Collaboration given the analysis of the dynamic fluctuations in the inclusive charged particle multiplicity for Au+Au collisions at $\sqrt{s_{NN}}$=200 GeV within the pseudo-rapidity range of $-3<\eta<3$[7, 8]. In their analysis an event-by-event observable C is used to study the multiplicity fluctuations.

$$C=\frac{N_1-N_2}{\sqrt{N_1+N_2}}\ ,$$

where N_1 and N_2 are the multiplicities in a pair of η bins with the same bin size and symmetric with respect to $\eta=0$. The width of the C distribution ($\sigma(C)$) is used as their fluctuations observables. Because the difference of the two multiplicities is used in the definition of C and the two multiplicities change in the same direction when $N_{\rm part}$ varies from event to event, the $N_{\rm part}$ fluctuations are suppressed in the measured $\sigma(C)$. Also because of the event-by-event normalization factor $\sqrt{N_1+N_2}$ in the denominator, $\sigma(C)=1$ for independent particles. Thus non-1 $\sigma(C)$ indicates non-0 dynamic fluctuations in addition to the statistical fluctuations. The multiplicity fluctuations $\sigma^2(C)$ can be decomposed into two parts: statistic fluctuation ($\sigma^2_{\rm stat}$) and dynamic fluctuation ($\sigma^2_{\rm dyn}$). While the statistical fluctuations are due to the finite multiplicity, the dynamic fluctuations are related to the intrinsic correlations in the particle production. The long range (particle from different bins) correlations and the short range (particles usually in the same bin) have different effects in $\sigma^2(C)$ and different signs of the dynamic fluctuations.

Figure 3 top shows the $\sigma(C)$ dependence on the separation in η space with fixed η bin size 0.5. The data and reconstructed simulation (HIJING+GEANT) are similar. Both have a non-monotonic dependence on η because of the presence of the detector effects. The HIJING $\sigma(C)$ is slightly greater than 1, with the difference between the $\sigma(C)$ and 1 increasing with the η separation. This indicates that the dynamic fluctuations of HIJING are great than 0. The suppression in the mid-rapidity region is due to the fact that negative long range effect of the short range correlated particles selected into different bins cancels the positive short range correlations effect. Fig. 3 Bottom shows the $\sigma(C)$ dependence on the η bin size with the η centered at 2.0. The data and reconstructed simulation(HIJING+GEANT) are again similar. The HIJING $\sigma(C)$ increases with the η bin size. Such dependence on the bin size is a typical feature of particle correlations with finite correlation length. The data and reconstructed simulation $\sigma(C)$ also have the same trend of increasing with η bin size.

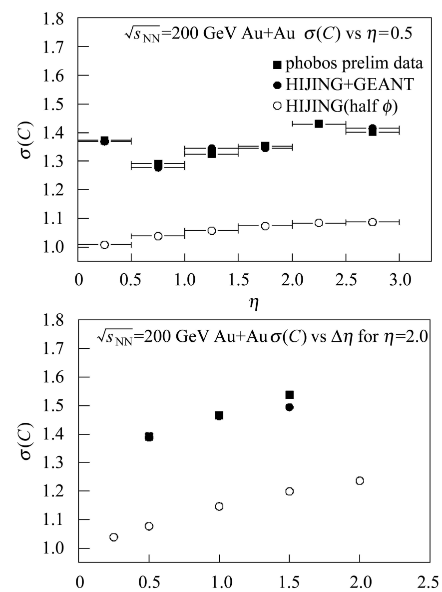

Fig. 3. Top: $\sigma(C)$ versus η with fixed η bin size 0.5. All values of $\sigma(C)$ are calculated using 50% azimuthal acceptance. The estimated systematic error of 5% is not shown in the plot. Bottom: $\sigma(C)$ versus $\Delta\eta$ with η bin centered at 2.0. All values of $\sigma(C)$ are calculated using 50% azimuthal acceptance. The estimated systematic error of 5% is not shown in the plot.

2.2 Fluctuations of particle ratios

NA49 Collaboration gave the first measurement of fluctuations from event to event in the production of strange particles in collisions of heavy nuclei. The ratio of charged kaons to charged pions is determined for individual central Pb+Pb collisions[9] (see Fig. 4 top).

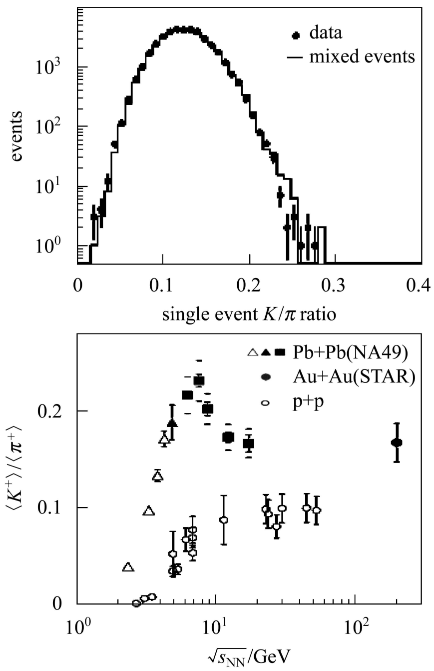

Fig. 4. Top: Distribution of the event-by-event kaon to pion ratio estimated using a maximum likelihood method (points). As a reference, the same procedure is applied to a mixed event sample (histogram) . Bottom: Energy dependence of full phase space $\langle K^+\rangle/\langle\pi^+\rangle$ and $\langle K^-\rangle/\langle\pi^-\rangle$ ratios in central Pb+Pb (Au+Au) collisions. The results of NA49 are indicated by squares. The data for p+p interactions are shown by open circles for comparison.

To quantify the remaining difference between data and mixed event the strength of non-statistical fluctuations is defined as

$$\sigma_{\text{non-stat}} = \sqrt{\sigma^2_{\text{data}} - \sigma^2_{\text{mixed}}}\ .$$

In general, processes leading to a correlated production of one or the other particle species or to a correlation in their multiplicities would result in $\sigma_{\text{non-stat}} > 0$, and they obtain

$$\sigma_{\text{non-stat}} = 2.8\ .$$

The results of the NA49 energy scan program show a sharp maximum of the ratio of K^+ to π^+ yields in the central Pb+Pb collisions at beam energies of 20—30 AGeV. (see Fig. 4 bottom)

This observation was interpreted as an indication of a phase transition at low SPS energies. The NA49 Collaboration presented the results on energy dependence of event-by-event fluctuations of the kaon to pion and proton to pion ratios at beam energies close to this maximum and complemented this study with preliminary data from the STAR Collaboration in the RHIC energy range. A significant increase of the fluctuation signal of the kaon to pion ratio at 20 and 30 AGeV is observed while it stays constant from the highest SPS energies out to the RHIC energy range[10] (See Fig. 5 and Fig. 6).

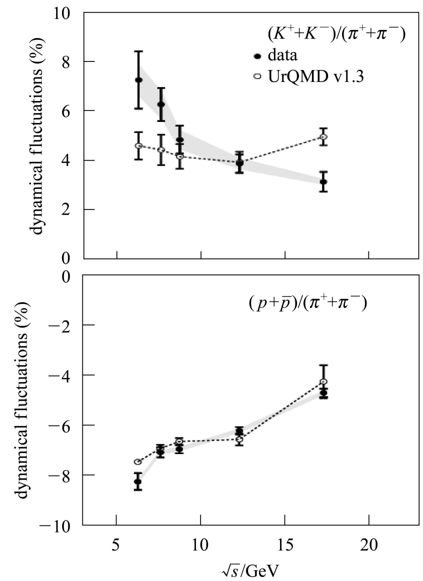

Fig. 5. Energy dependence of the event-by-event fluctuation signal of the $[K^++K^-]/[\pi^++\pi^-]$ ratio (top) and the $[p+\bar{p}]/[\pi^++\pi^-]$ ratio(bottom). The systematic errors of the measurements are shown as gray bands.

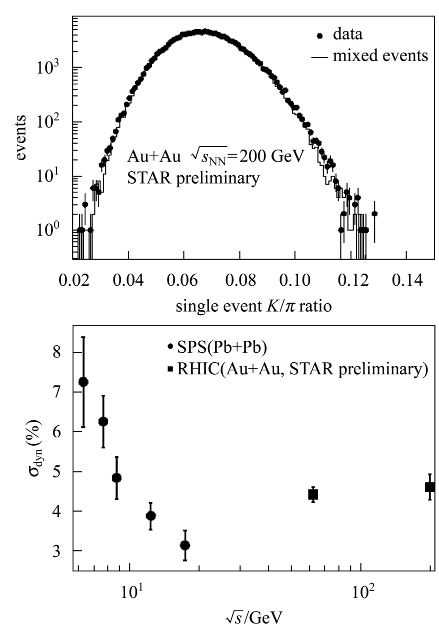

Fig. 6. Preliminary data obtained by the STAR Collaboration. Top: Distribution of K/π ratio from data and mixed events for Au+Au at $\sqrt{s_{\text{NN}}}$=200 GeV. Bottom: Energy dependence of the event-by-event fluctuation signal of the $[K^++K^-]/[\pi^++\pi^-]$ ratio.

The STAR experiment also measured the centrality dependence of dynamical fluctuation in K/π ratio in Au+Au collisions in 200 GeV at RHIC[10] (see Fig. 7).

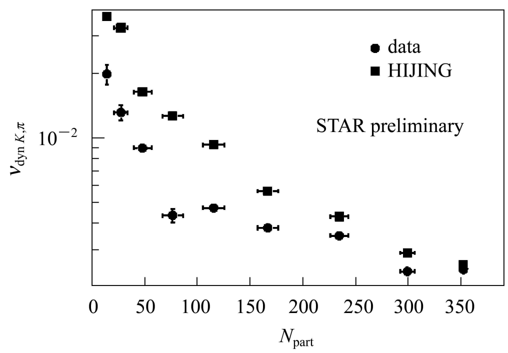

Fig. 7. Centrality dependence of dynamical fluctuation.

2.3 Transverse momentum (p_t) fluctuations and correlations

$\langle p_t\rangle$ fluctuations are expected to reflect the variations of global temperature T assuming that each collision achieved a thermalized final state, with a different "temperature" for each event. More generally, $\langle p_t\rangle$ fluctuations result from event-wise changes in the (η,ϕ) dependence of the shape of the single-particle p_t spectrum.

2.3.1 $\langle p_t\rangle$ fluctuation measures

Initial fluctuation measures assumed that a few global event variables could fully characterize the thermalized heavy ion collisions. Comparing the variance of a global variable with a statistical reference should then extract all available information. $\langle p_t\rangle$ was intended to estimate a global temperature. It should fluctuate with a "statistical" component and a component reflecting collision dynamics in some way to be determined. Comparing $\sigma^2_{\langle p_t\rangle}$ to $\sigma^2_{\hat{p}_t}/\bar{n}$ as a central-limit reference (independent p_t samples from a fixed parent spectrum) should then constitute a complete fluctuation measurement and reveal 'dynamical' collision details.

Several fluctuation measures defined at the SPS and RHIC were based on those expectations, e.g., in Ref. [11]

$$\sigma^2_{p_t,\mathrm{dynamical}}\equiv\sigma_{\langle p_t\rangle}-\sigma^2_{\hat{p}_t}/\bar{n}$$

and in Refs. [12, 13]

$$F_{p_t}\equiv\sigma_{\langle p_t\rangle,\mathrm{data}}/\sigma_{\langle p_t\rangle,\mathrm{mixed}}-1\ ,$$

with $\sigma_{\langle p_t\rangle,\mathrm{mixed}}\approx\sigma^2_{\hat{p}_t}/\bar{n}$. Because $\langle p_t\rangle=p_t/n$ is a ratio of random variables its variance becomes anomalously large for small $\bar{n}$, an example of measure bias. Both the above measures respond to n fluctuations as well as true p_t fluctuations and are dominated by a term proportional to $\sigma^2_n/\bar{n}^2\approx1/\bar{n}$ for small $\bar{n}$. A variant of $\sigma^2_{p_t,\mathrm{dynamical}}$,

$$\langle\delta p_{ti}\cdot\delta p_{tj}\rangle=\overline{\left\{\frac{\Sigma_{i\neq j}(p_{ti}-\hat{p}_t)(p_{tj}-\hat{p}_t)}{n(n-1)}\right\}}^{[14]}\ ,$$

substantially reduces bias, but at the expense of playing a role intermediate between fluctuation and correlation measurement which makes its interpretation difficult. Further adding to confusion are the approximate relations among fluctuation measures which may be valid in a large-n limit but fail for small multiplicities. Attempts to 'simplify' the statistical measure landscape with such approximations have impeded progress in fluctuation/correlation analysis.

$\Phi_{p_t}\equiv\sqrt{\overline{(p_t-n\hat{p}_t)^2}/\hat{n}}-\sqrt{\sigma^2_{\hat{p}_t}}$ tests invariance of $\langle p_t\rangle$ fluctuations under superposition of independent systems[15], e.g., p-p linear superposition compared with A-A collisions[16—18]. A closely-related measure is based on Pearson's normalized covariance[19]

$$r_{ab}\equiv\frac{\sigma^2_{ab}}{\sqrt{\sigma^2_a\sigma^2_b}}\to\frac{\overline{(p_t-n\hat{p}_t)_a(p_t-n\hat{p}_t)_b}}{\sigma^2_{\hat{p}_t}\sqrt{\bar{n}_a\bar{n}_b}}$$

which has the same property. The STAR Collaboration drops $\sigma^2_{\hat{p}_t}$ from the denominator to be consistent with other measures, takes $a=b$ and obtains

$$\Delta\sigma^2_{p_t:n}\equiv\overline{(p_t-n\hat{p}_t)^2}/\bar{n}-\sigma^2_{\hat{p}_t}$$

a comparison between a normalized variance and its central-limit (CLT) Refs. [16, 20]. $\Delta\sigma^2_{p_t:n}$ is a variance difference whereas Φ_{p_t} is a difference between r.m.s terms. In general, variances and covariances obey a linear algebra, and $\Delta\sigma^2_{p_t:n}$ is simply related to two-particle correlations.

Σ_{p_t} is motivated by a specific model of global temperature fluctuations in thermalized events. There are two versions:

$$\Sigma_{p_t}\equiv\sqrt{\Delta\sigma^2_{p_t:n}/\bar{n}\hat{p}_t^{\,2}}^{\ [17]}$$

and

$$\Sigma'_{p_t}\equiv\sqrt{\langle\delta p_{ti}.\delta p_{tj}\rangle/\hat{p}_t^{\,2}}^{\ [14]}\ .$$

If the hypothesis of global thermalization underlying these definitions is not valid the meaning of either Σ_{p_t} is not clear. The STAR Collaboration finds plentiful evidence that the global thermalization is not satisfied in RHIC collisions.

2.3.2 $\langle p_t\rangle$ fluctuation measurements

The first $\langle p_t\rangle$ fluctuation measurement, made by NA49 at the SPS for the central Pb+Pb collisions at 17.3 GeV[21], is shown in Fig. 8. A frequency curve on $M(p_t)=\langle p_t\rangle$ (points) is compared with a mixed-pair reference (histogram). A quantitative comparison between data and reference was made with Φ_{p_t}[15]. They got $\Phi_{p_t}=0.6\pm1.0$ MeV/c, compatible with zero. This means that no significant non-statistical fluctuations were observed in the rapidity acceptance.

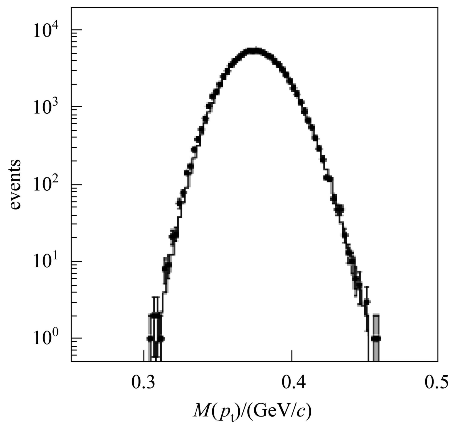

Fig. 8. Frequency distribution on $M(p_t) = \langle p_t \rangle$ measured by NA49 at 17.3 GeV.

The second measurement at the SPS was carried out by CERES. The results are shown in Fig. 9[22]. A significant fluctuation excess was observed within a rapidity acceptance centered at the CM. That result is also notable as the first measurement of the scale or bin-size dependence of fluctuations (on η). The data in the middle panel permit partial reconstruction of the p_t angular correlation which produces $\langle p_t \rangle$ fluctuation at the SPS, an important SPS result.

In Ref. [22] it was argued that the similarity between the first and second panels implies that Φ_{p_t} is "proportional to" multiplicity, apparently a design defect of that measure, whereas $\sigma^2_{p_t,\mathrm{dynamical}} \approx 2\sigma_{\hat{p}_t}\Phi_{p_t}/\bar{n}$ supposedly eliminates the offending factor $\bar{n}$. In fact, $\bar{n}$ and Φ_{p_t} are the running integrals on scale of one- and two-particle momentum space and correctly reflect the structure of those spaces. $\sigma^2_{p_t,\mathrm{dynamical}}$, the ratio of two running integrals, is therefore a running average of the underlying two-particle correlation (autocorrelation) which therefore presents a distorted picture of p_t angular correlations and suppresses the localized p_t structure such as mini-jets.

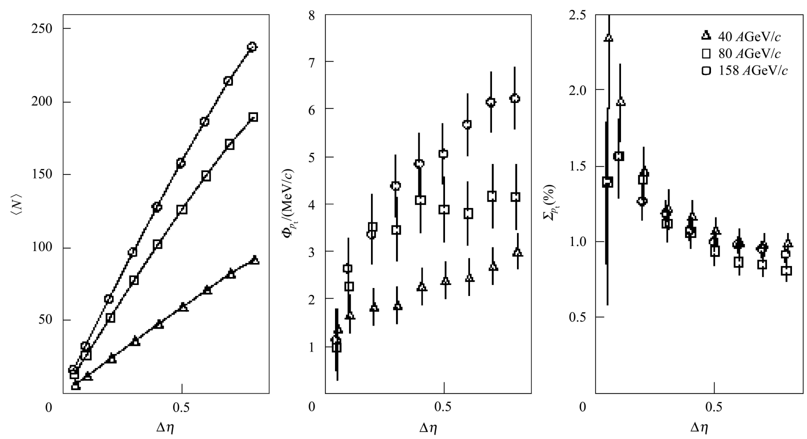

Fig. 9. The mean charged particle multiplicity $\langle N \rangle$ (left) and the fluctuation measures Φ_{p_t} (middle) and Σ_{p_t} (right) in central Pb+Au event at 40,80, and 158 A GeV/c as a function of the pseduorapidity bin size $\Delta\eta$. The center of the $\Delta\eta$ window is always fixed at $\eta = 2.45$.

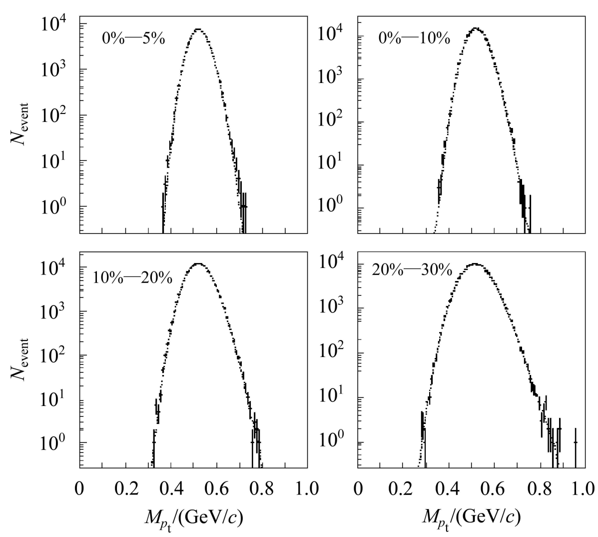

Fig. 10. The M_{p_t} distribution for all centrality classes. The curves are the random baseline mixed event distributions.

An initial null result was given by PHENIX[12]. Distributions of event-by-event fluctuations of the mean transverse momentum and mean transverse energy near mid-rapidity have been measured in Au+Au collisions at $\sqrt{s_{\rm NN}}$=130 GeV at the RHIC. By comparing the distributions with what is expected for statistically independence particle emission, the magnitude of nonstatistical fluctuation in mean transverse momentum is determined to be consistent with zero (see Fig. 10).

After an initial null result[12], measurements by PHENIX provided the first indication of nonzero $\langle p_{\rm t}\rangle$ fluctuations at RHIC[13](see Fig. 11 and Fig. 12). The increase of $F_{p_{\rm t}}$ with increasing $p_{\rm t}$ implies that the majority of the fluctuations are due to correlated high $p_{\rm t}$ particles. A Monte Carlo simulation that includes elliptic flow and a PYTHIA-based hard-scattering description can consistently describe contributions to the signal as a function of centrality and $p_{\rm t}$ with a simple implementation of jet suppression.

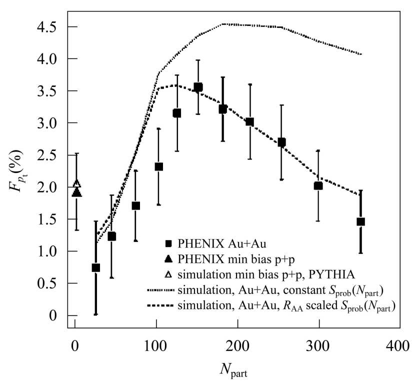

Fig. 11. $F_{p_{\rm t}}$ (in percent, 0.2 GeV/c< $p_{\rm t}$ < 2.0 GeV/c) as a function of centrality, which is expressed in terms of the number of participants in the collision, $N_{\rm part}$. The solid squares represent the Au+Au data. The solid triangle represents the minimum bias p+p data point. The open triangle is the result from an analysis of PYTHIA minimum bias p+p events within the PHENIX acceptance. The error bars include statistical and systematic errors and are dominated by the latter. The curves are the results of a Monte Carlo simulation with hard processes modeled using PYTHIA with a constant (dotted curve) and $R_{\rm AA}$-scaled (dashed curve) hard-scattering probability factor, and include the estimated contribution due to elliptic flow.

Extensive measurements of several aspects of $\langle p_{\rm t}\rangle$ fluctuations have been carried out by the STAR Collaboration[14,16,17,23]. Fig. 13 (upper panel) presents a STAR measurement of the frequency distribution on $\sqrt{n}(\langle p_{\rm t}\rangle - \hat{p_{\rm t}})/\sigma_{\hat{p_{\rm t}}}$ (histogram) for Au+Au collisions at 130 GeV compared with a central-limit reference in the form of a gamma distribution (narrow curve)[16]. The variance excess is obvious for this measurement in the STAR angular acceptance. The lower panel shows the difference between data and reference in the upper panel relative to the statistical error $\sqrt{N}$. The large statistical significance of the variance excess is indicated by deviations of up to 20 standard deviations in each histogram bin. That STAR

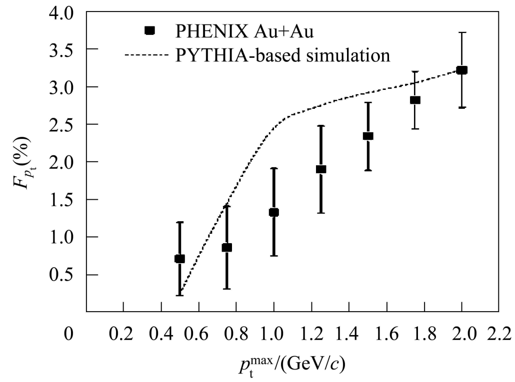

Fig. 12. $F_{p_{\rm t}}$ (in percent) of nonrandom fluctuation as a function of the $p_{\rm t}$ range over which $M_{p_{\rm t}}$ is calculated, 0.2 GeV/c< $p_{\rm t}$ < $p_{\rm t}^{\rm max}$, for the 20%—25% centrality class ($N_{\rm part}$=181.6). The curve is the result of a Monte Carlo simulation with hard-scattering process modeled using PYTHIA with $S_{\rm prob}(N_{\rm part})$=0.075 and $R_{\rm AA}=0.41$. The error bars include statistical and systematic errors and are dominated by the latter. The contribution of elliptic flow is estimated to be negligible at this centrality.

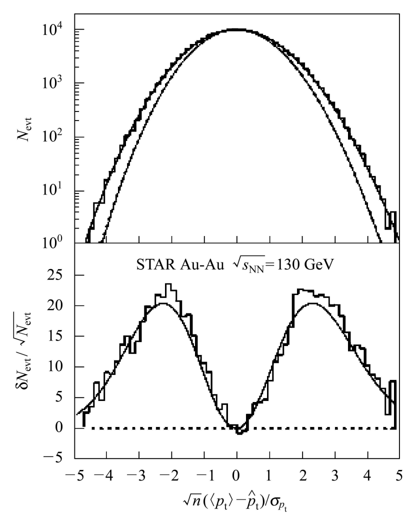

Fig. 13. Upper panel: Event frequency distribution on $\sqrt{n}(\langle p_{\rm t}\rangle - \hat{p_{\rm t}})/\sigma_{\hat{p_{\rm t}}}$ for 80% of primary charged hadrons in $|\eta|$ < 1 for 183K central events (histogram) compared with gamma reference (dashed curve). Monte Carlo reference (solid curve underlying gamma reference), and broadened distribution (solid curve underlying data, not a fit). Lower panel: difference in upper panel between data and gamma reference (histogram) or between broadened distribution and gamma reference (solid curve) normalized by the Poisson error $\sqrt{N_{\rm evt}}$ in each bin.

result suggests that the unexpected phenomena might be present in RHIC collisions and the initiated an era of precision differential measurements of p_t fluctuations and correlations.

Figure 14 shows the variation of difference factor $\Delta\sigma_{p_t:n} \approx \Phi_{p_t}$ with centrality, measured by particle multiplicity N relative to reference N_0 (for b=0, central collisions). $\Delta\sigma_{p_t:n}$, defined by $\Delta\sigma^2_{p_t:n} \equiv 2\sigma_{\hat{p_t}}\Delta\sigma_{p_t:n}$[16], facilitates comparison with Φ_{p_t}[15]. The centrality dependence is smooth, inconsistent with discontinuities expected by some to signal traversal of the quark-gluon plazma (QGP) phase boundary.

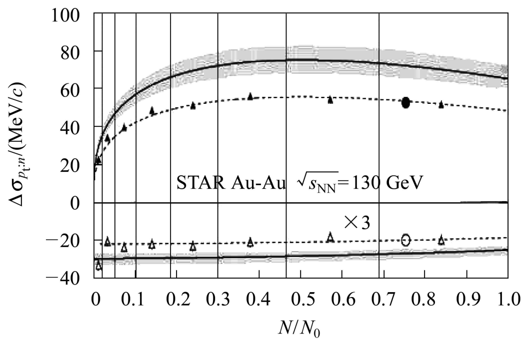

Fig. 14. Mean-p_t difference factors $\Delta^{CI}_{p_t;n}$ and $\Delta^{CD}_{p_t;n}$ for 205K minimum-bias Au+Au events at $\sqrt{s_{NN}}$ = 130 GeV vs relative multiplicity N/N_0, which is approximately $N_{part}/N_{part,max}$, the relative fraction of participant nucleons. Charge-independent (CI) (solid triangular points) and charge-dependent (CD) (open triangular points, multiplied by 3 for clarity) difference factors include statistical errors only (smaller than symbols). Parametrization (dashed curves), extrapolation of parametrization to true primary particle number (solid curves), and systematic uncertainties (bands) are discussed. Difference factors for the 15% most-central collision events are shown by the solid circle and open circle symbols.

Figure 15 shows the energy dependence of the transverse momentum correlations, $\langle\Delta p_{t,i}\Delta p_{t,j}\rangle$ (top panel), the correlations multiplied by the multiplicity density (middle panel) and the square root of the correlations divided by the event-wise average transverse momentum per event (bottom panel), as a function of event centrality for Au+Au collision[14].

Given the close connection between parton scattering and $\langle p_t\rangle$ fluctuation at RHIC the collision energy dependence of $\langle p_t\rangle$ fluctuation could reveal previously inaccessible parton dynamics at lower (e.g., SPS) collision energies. The STAR Collaboration gives the first study of the energy dependence of p_t angular correlations inferred from event-wise mean transverse momentum $\langle p_t\rangle$ fluctuation in heavy ion collisions[23]. They compare their large-acceptance measurements at CM energies $\sqrt{s_{NN}}$= 19.6, 62.4, 130 and 200 GeV with SPS measurements at 12.3 and 17.3 GeV[22]. In Fig. 16 Top the pseudorapidity scale (bin size) dependence of fluctuations at full azimuth acceptance is shown for central collisions at six energies. In the Bottom they show the centrality dependence of $\langle p_t\rangle$ fluctuation for four RHIC energies and a summary (crosshatched region) of SPS fluctuation measurements. Φ_{p_t} was used for the CERES fluctuation measurements[22]. To good approximation $\Delta\sigma_{p_t:n} \approx \Phi_{p_t}$ and both are per particle fluctuation measures which test linear superposition. For either measure we observe a dramatic increase in $\langle p_t\rangle$ fluctuation from SPS to RHIC energies. The scale dependence in the first panel illustrates how measurements with different detector acceptances are related. The centrality dependence in the second panel suggests that fluctuations in p-p and peripheral A-A collisions saturate at and above 60 GeV, whereas there is monotonic increase for the more central collisions.

At the higher RHIC energies $\langle p_t\rangle$ fluctuations are dominated by fragments from low-Q^2 parton collisions. The energy dependence of $\Delta\sigma_{p_t:n}$ or Φ_{p_t} is shown in Fig. 17, plotted vs $\sqrt{s_{NN}}$[23]. The $\langle p_t\rangle$ fluctuation in cental collisions varies almost linearly as $\log\{\sqrt{s_{NN}}/10\text{ GeV}\}$ (solid line in the panel), suggesting a threshold for observable transverse parton scattering and fragmentation near 10 GeV.

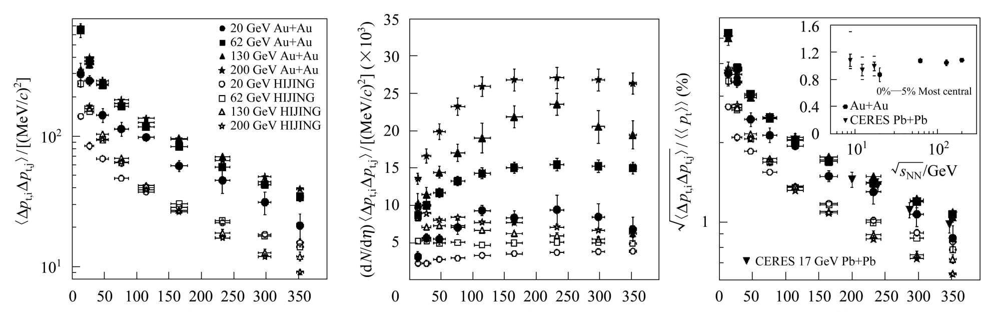

Fig. 15. $\langle\Delta p_{t,i}\Delta p_{t,j}\rangle$ (left), $(\mathrm{d}n/\mathrm{d}\eta)\langle\Delta p_{t,i}\Delta p_{t,j}\rangle$ (middle) and $\sqrt{\langle\Delta p_{t,i}\Delta p_{t,j}\rangle}/\langle\langle p_t\rangle\rangle$ (right) as a function of centrality and incident energy for Au+Au collisions compared with HIJING results.

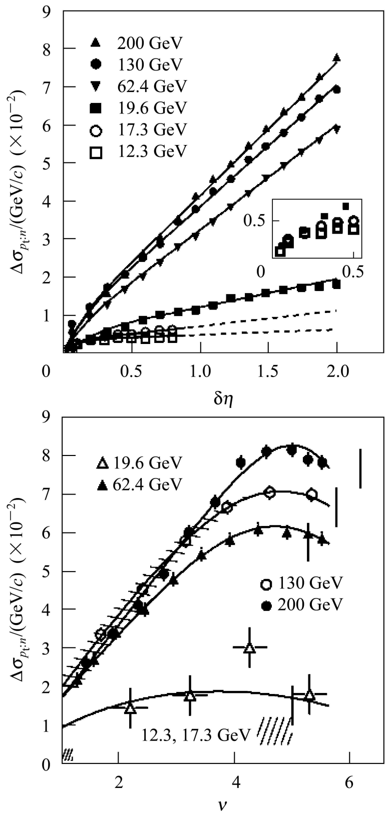

Fig. 16. Top: Per-particle fluctuation dependence on pseudorapidity scale $\delta\eta$ in central collisions. STAR measurements are solid symbols, CERES measurements are open symbols. The inset shows details at small $\delta\eta$. Bottom: Centrality dependence for four energies. ν is the mean participant path length[24]. The vertical line at right estimates ν for $b=0$. The upper hatched band estimates the uncertainty in ν for 130 GeV data. There is an overall 14% systematic error in the corrected amplitudes. SPS measurements of Φ_{p_t} at 12.3 and 17.2 GeV (the lower-right hatched region, with errors and centrality range) are included for comparison.

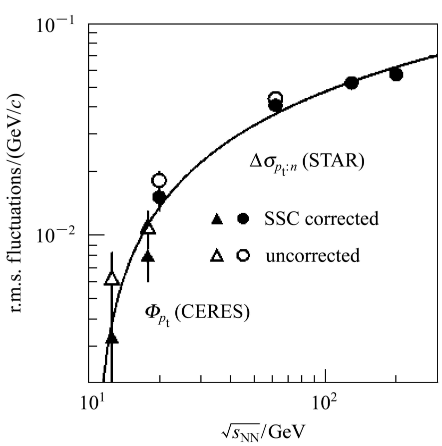

Fig. 17. Energy dependence of $\langle p_t \rangle$ fluctuation for Au+Au collisions in the STAR acceptance.

2.3.3 $\langle p_t \rangle$ fluctuation scale dependence and inversion

To answer the question "what phenomena produce $\langle p_t \rangle$ fluctuations" The STAR Collaboration defines the relation between fluctuations and correlations. Fig. 18 (top left panel) shows $\Delta\sigma^2_{p_t:n}(\delta\eta,\delta\phi)$-the p_t variance excess distribution on angular scales $(\delta\eta,\delta\phi)$. A fluctuation measurement at the full STAR TPC acceptance corresponds to the single point at the apex of the distribution on scale. Other points on the surface correspond to divisions of the acceptance into successively smaller bins. The surface is structured and contains information on underlying p_t correlations, but the meaning is still not clear.

Fluctuations in bins of a given size or scale are determined by two-particle correlations with characteristic lengths less than or equal to the bin scale. By measuring the fluctuation magnitudes as a function of bin size one can recover some details of the underlying two-particle correlation structure-those aspects which depend on the separation of pairs of points, not on their absolute positions. The relation between fluctuations and correlations is given by the integral equation

$$\Delta\sigma^2_{p_t:n}(m\epsilon_\eta,n\epsilon_\phi)=4\sum_{k,l=1}^{m,n}\epsilon_\eta\epsilon_\phi K_{mn;kl}\frac{\Delta\rho(p_t:n;k\epsilon_\eta,l\epsilon_\phi)}{\sqrt{\rho_{\rm ref}(n;k\epsilon_\eta,l\epsilon_\phi)}},$$

with kernel $K_{mn;kl}\equiv(m-k+1/2)/m.\ (n-l+1/2)n$ representing the 2D macro-bin system. $\Delta\sigma^2_{p_t:n}(\delta\eta,\delta\phi)$ is a variance excess, and $\Delta\rho(p_t:n;)/\sqrt{\rho_{\rm ref}(n)}$ is a normalized covariance density. That equation can be solved to obtain the p_t angular autocorrelation.

Figure 18 (top right panel) shows the angular autocorrelation on different axes $(\eta_\Delta,\phi_\Delta)$ (e.g., $\eta_\Delta=\eta_1-\eta_2$) obtained by inverting the fluctuation scale dependence in the first panel. There are two major features: a sinusoid corresponding to "elliptic flow" and non-sinusoidal structure called "non-flow" in conventional flow terminology. This is the first observation of flow as a p_t correlation or velocity structure[17]. The sinusoid can be removed precisely, leaving the structure in the bottom left panel which is dominated by mini-jet correlations, especially a same-side positive peak[17]. In the bottom right panel they plot the same angular autocorrelation on $(\eta_\Delta,\phi_\Delta)$ in a cylinder format.

From the example in Fig. 18 we can see that inversion of p_t fluctuation scale dependence to an autocorrelation provides direct physical interpretation of p_t fluctuation mechanisms. Parton fragment distributions (mini-jets) are visualized as event-wise temperature/velocity structures on (η,ϕ). A comprehensive picture of parton scattering, dissipation and fragmentation in heavy ion collisions is thereby established.

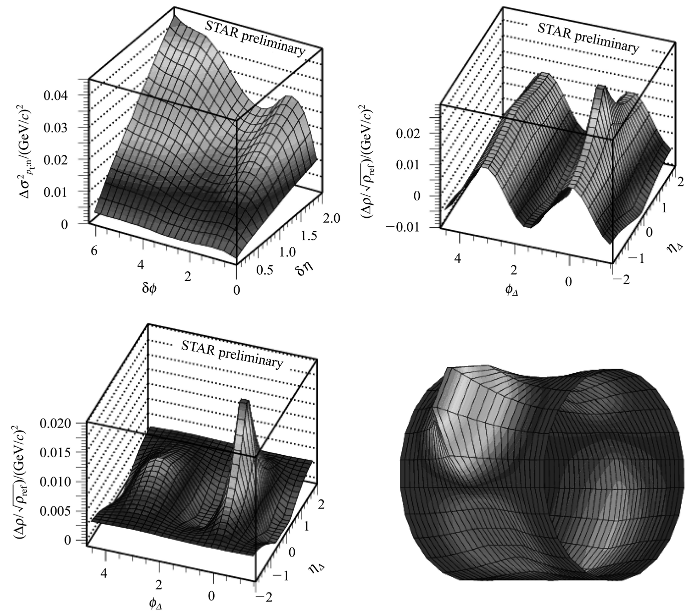

Fig. 18. $\langle p_{\rm t}\rangle$ fluctuation scale dependence on (η,ϕ) for $\sqrt{s_{\rm NN}}$=200 GeV mid-central Au-Au collisions measured by STAR (top left); corresponding $p_{\rm t}$ angular autocorrelation obtained by inversion (top right); the same autocorrelation after subtracting the elliptic flow contribution (bottom left); the same data plotted in cylinder format (bottom right).

2.4 HBT

The experimental technique of using two-particle interferometry to relate the momentum space separation of particles to their separation in space-time is well established[25]. In the case of identical bosons, e.g. π^+ mesons, quantum interference among the particles leads to an enhancement of pairs with small momentum difference $\boldsymbol{q}$ (Bose-Einstein enhancement). To isolate the small set of correlated pairs that undergo this quantum interference from the enormous amount of uncorrelated pairs in an event, a correlation function $C(\boldsymbol{q})$ is formed in which pairs from real events are divided by pairs from different events. In heavy-ion collisions, $C(\boldsymbol{q})$ is often constructed in three dimensions and fit to a three-dimensional Gaussian:

$$C(q) = \frac{\text{real}-\text{pairs}}{\text{mixed}-\text{pairs}} = N[1+\lambda \mathrm{e}^{-q_{\rm out}^2 R_{\rm out}^2 - q_{\rm side}^2 R_{\rm side}^2 - q_{\rm long}^2 R_{\rm long}^2}],$$

where the subscripts indicate the long (parallel to beam), side (perpendicular to beam and total pair momentum $\boldsymbol{K}$) and out (perpendicular to $q_{\rm long}$ and $q_{\rm side}$) decomposition of $\boldsymbol{q}$. N is a normalization constant. The R's in the above equation, known as the HBT radii, quantify the widths of the Gaussians and represent the apparent size of the particle source, which may depend on the transverse momentum slice under study. In practice, the final-state effect such as Coulomb also contributes to $C(\boldsymbol{q})$ and needs to be accounted for.

The purpose of HBT studies in heavy-ion collisions is to explore the space-time evolution and freeze-out of the system, This can be thought of as three-fold: the spatial distribution of the emission points, the time length of emission, and the dynamical properties of the system as it evolves. HBT serves as a tool for disentangling these contributions, and the out-side-long decomposition of $\boldsymbol{q}$ is chosen for that reason. Experimentally, HBT radii are studied as differentially as statistics and detector configurations allow; see Table 1[26].

Table 1. Some of the HBT differential studies underway recently in heavy-ion collisions.

Diff. quantity	what it investigates
beam energy	onset effects, transition phenomena
transverse momentum	dynamics, collective expansion
particle type	hydrodynamic $m_{\rm T}$ scaling
collision system	origin of Bose-Einstein enhancement
azimuthal angle	spatial anisotropy, system evolution

We will highlight these five differential studies here.

2.4.1 Beam energy

CERES Collaboration had presented a systematic study of two-pion interferometry data at SPS energies[27]. A detailed study of the Bertsch-Pratt BHT radius parameters has been performed as function of the mean pair transverse momentum $k_{\rm t}$ and

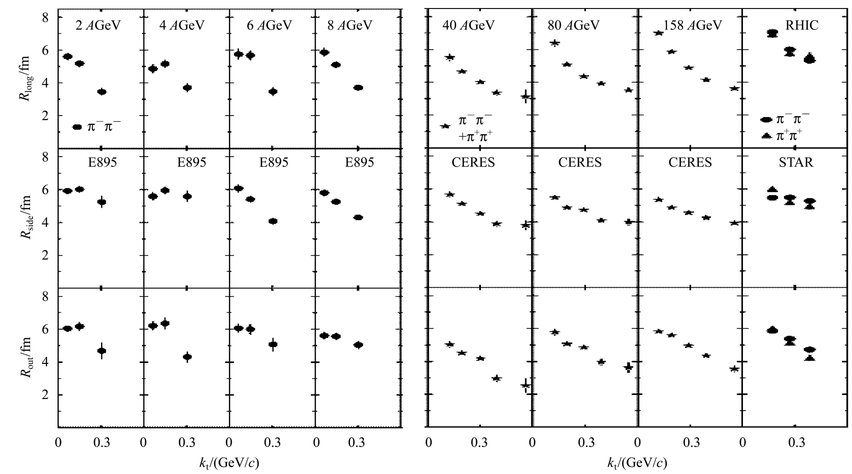

Fig. 19. Compilation of HBT radius parameters near midrapidity in central Pb(Au)+Pb(Au) collisions at AGS[28], SPS[27] and RHIC[29] energies.

in bins of the centrality of the collision. Pion interferometry data published by experiments at AGS and RHIC together with the SPS data can be combined to perform a systematic study of the source parameters over a wide range of beam energies. Fig. 19 are shows the $k_{\rm t}$-dependence of $R_{\rm long}$, $R_{\rm side}$, and $R_{\rm out}$ in central Pb(Au)+Pb(Au) collisions near midrapidity[28, 29]. No dramatic variation of the source parameters can be observed. However, a closer inspection reveals interesting features. The parameter $R_{\rm long}$ is approximately constant from AGS to the lower SPS energies, but starts to increase significantly within the SPS regime and towards RHIC, indicating a smooth increase of the lifetime. $R_{\rm side}$ is gradually decreasing at small $k_{\rm t}$ up to top SPS energy, connected with a continuous flattening of the $k_{\rm t}$-dependence. At RHIC, $R_{\rm side}$ is again larger than at the SPS while the shape is not yet well measured. The parameter $R_{\rm out}$ shows a rather weak energy dependence and a slight minimum around the lowest SPS energy, where $R_{\rm out}/R_{\rm side} < 1$.

An investigation of the freeze-out conditions can be performed by relating the measured source parameters to an effective freeze-out volume:

$$V_{\rm f} = (2\pi)^{3/2} R_{\rm long} R_{\rm side}^2 \ ,$$

computed for Gaussian density distributions in all three spatial dimensions. In the presence of collective expansion, $V_{\rm f}$ does not comprise the total volume of the pion source at freeze-out but rather reflects a volume of homogeneity. If thermal freeze-out would occur at constant density, a linear scaling of $V_{\rm f}$ with the charged particle multiplicity would be expected. Fig. 20 shows $V_{\rm f}$, computed at $0.15 < k_{\rm t} < 0.25$ GeV/c, as a function of the number of participants at 40, 80, and 158 AGeV. The centrality dependence of the effective freeze-out volume $V_{\rm f}$ is consistent with the assumption of pion freeze-out at constant particle density. However, this simple picture breaks down if different beam energies are compared. The key to understand this effect is the consideration of the cross sections of different particle species with pions, as the relative abundances change with beam energy.

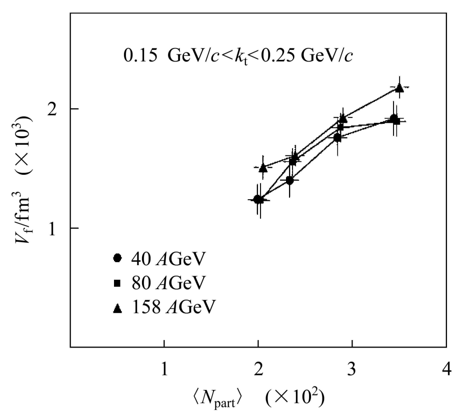

Fig. 20. The freeze-out volume $V_{\rm f}$ calculated at $0.15 < k_{\rm t} < 0.25$ GeV/c as a function of the centrality expressed here in terms of the number of participants at 40, 80, and 158 AGeV.

The STAR Collaboration at RHIC shows the result[29] that the pion interferometry excitation function for the heaviest ions spans nearly two decades in $\sqrt{s_{\rm NN}}$[30—32]. No sudden jumps in HBT radii were observed (see Fig. 21), but lower energy RHIC measurements were needed to complete the search for a predicted increase in emission time scale related to the possible onset of QGP formation.

2.4.2 Transverse momentum

The transverse momentum ($k_{\rm t}$) dependence of the HBT radii for identical pions probably is studied most often, under the model-dependence view that space-momentum correlations in the source are due mostly to collective expansion[25]. As the source expands, radial flow pushes higher $p_{\rm t}$ particle more at surface. Within this picture, analytical expressions have been derived to extract the expansion velocity and emission duration from the $m_t(m_t = \sqrt{p_t^2+m^2})$ dependence of the HBT radii.

The hydrodynamical approach to understanding HBT is motivated at RHIC by the model's demonstrated ability to describe soft p_t spectra and elliptic flow consistently for several particle species[33]. "Hydro" calculations for these observables point to fast thermalization in a partonic phase, followed by hydrodynamic expansion for ~15 fm/c with an intermediate phase transition. However, these calculations yield strong disagreement with HBT radii[34]: $R_{\rm out}$ and $R_{\rm long}$ are overpredicted by as much as a factor of 2, and $R_{\rm side}$ is somewhat underpredicted. In particular, the measured k_t dependence of $R_{\rm side}$ is in contrast to hydro and other models that predict little (if any) k_t dependence. This disagreement, and the lack of energy dependence of the BHT radii for a fixed k_t bin[29], is known as the "HBT Puzzle".

Collective flow generates a characteristic fall-off of the pion source radii with k_t, which is ubiquitously observed in data. Final results for the k_t-dependence of Gaussian radii from central Au+Au (Pb+Pb) collisions exist at the AGS[28, 35], SPS[30, 36—39], and RHIC[29, 40—43]. As is clear from Fig. 22, aside from a small variation in overall scale, the k_t dependence is startlingly similar for all energies[44].

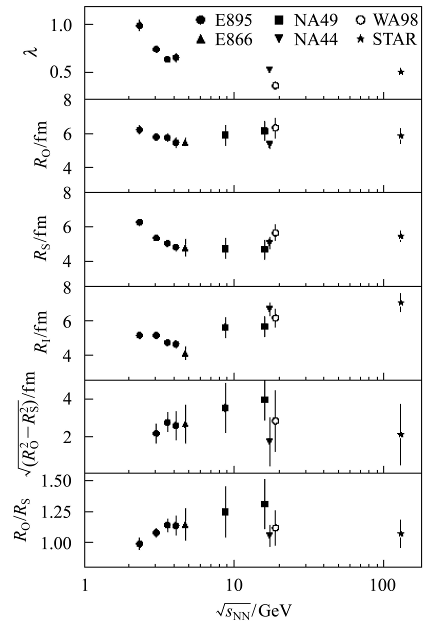

Fig. 21. The energy dependence of π^- HBT parameters for central Au+Au (Pb+Pb) collisions at midrapidity and $p_t \approx 0.17$ GeV/c[28, 30—32]. The SPS data are offset slightly in $\sqrt{s_{\rm NN}}$ for clarity.

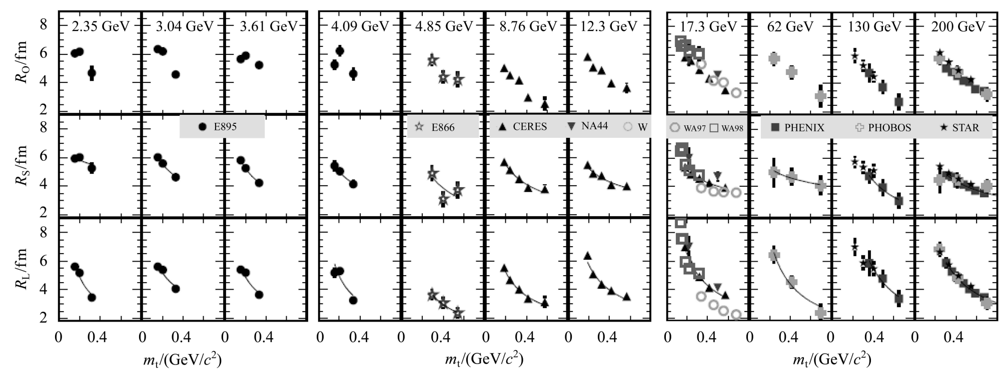

Fig. 22. World data set of published m_t dependence of pion Bertsch-Pratt radii near mid-rapidity from Au+Au (Pb+Pb) collisions. Centrality selection is roughly to 10% of cross-section, but varies somewhat with experiment. Lines represent parameterized fits.

2.4.3 Particle type

Systematic studies for different mass particles provide additional controls probing the space-time evolution of the source. Particularly for kaons, the interpretation may be simplified owing to the reduced effects of resonance feed-down[45] and a reduced scattering cross-section for K^+ in nuclear matter, and raising the possibility that kaon correlations could peer farther back to earlier stages of the collision[46]. Indeed, the first kaon measurements[47—50] reported smaller source radii for kaons. However, the observation shown that the radii for K^+ and K^- were very similar[48] was an early experimental indication that different cross-sections were not the driving physics behind these smaller radii. In this case, the smaller radii for kaons results from their increased mass in a flow field, not in different cross-sections.

If indeed the flow is generated in matter sufficiently dense that individual cross-sections are unimportant, then all particles participate equally in collective transverse flow. In this case, their source radii should approximately follow a common m_t scaling[51—54]. Within uncertainties, the first results on koan interferometry by NA44 at the SPS in S+Pb[55] and Pb+Pb[56] collisions were consistent with a $1/\sqrt{m_t}$ scaling.

Figure 23 collects the m_t dependence of homogeneity lengths for several energies. The left panels show the results for Si+Au collisions at $\sqrt{s_{NN}}$=5.4 GeV, measured by E802 for pions[57] and kaons[47, 49]. Femtoscopic radii for pions[30, 37, 39, 58], kaons[56], protons[59], and photons[60] measured in Pb+Pb collisions at the SPS are shown in the center panels. The right panel shows the one-dimensional radius parameter R_{inv} measured at RHIC for pions,charged kaons,and protons[61], neutral kaons[62], and with Λ-p correlations[63]. To compare across energies, R_{inv} results are included for the AGS and also for the SPS, where the R_{inv} values were calculated from 3D fit results by accounting for the boost along the outwards direction from the LCMS (in which $P_z=0$) to the PCOM (pair center-of-mass, in which $|\boldsymbol{P}|=0$) frame, $R^2_{inv}=R^2_{long}+R^2_{side}+\gamma^2R^2_{out}$, where γ is given by m_t/m of the pair. Note that for massless particles, such as photons, γ is given by k_t/Q_{inv}.

This consistency between different particle types may carry an important message. It calls into question theoretical scenarios which appear to explain $R_i(M_t)$ for particle type only. Further, the consistency with emission from a common flow-dominated source may also support freeze-out scenarios in which the last scattering in the dense phase determines the homogeneity region, instead of milder rescatterings in the more dilute stage, which are dominated by particle species-dependent cross-section.

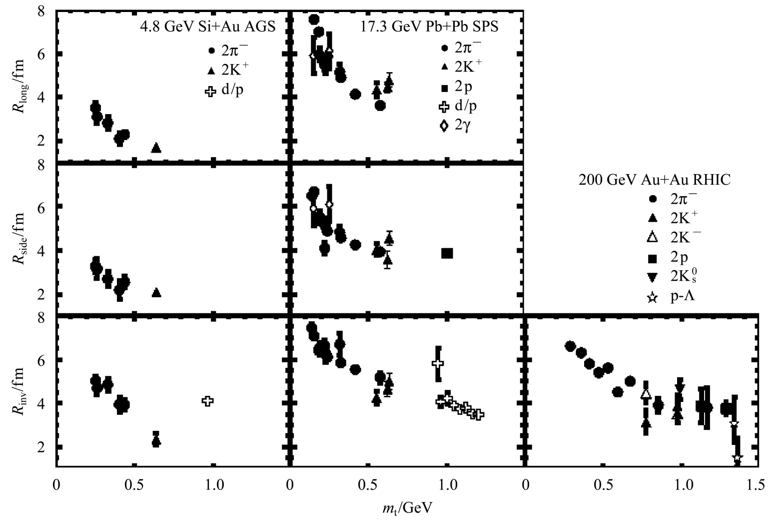

Fig. 23. Transverse mass dependence of homogeneity lengths from correlations between particles of identical mass.

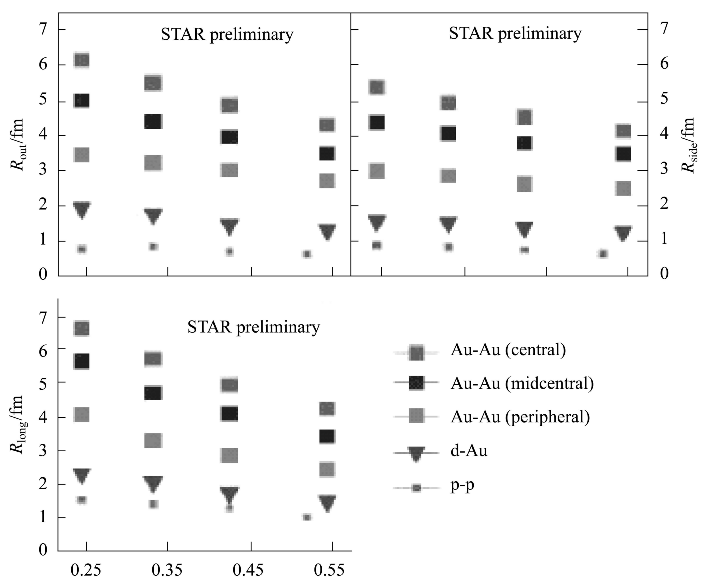

Fig. 24. The transverse mass dependence of the 3D Bertsch-Pratt radii in p+p, d+Au, and Au+Au at STAR. Three centralities are displayed for Au+Au.

2.4.4 Collision system

One of the advantages of the RHIC experimental program is the ability to collide different systems with the same center-of-mass energy, allowing for identical analysis of these different systems. The STAR Collaboration was given the preliminary results of pion HBT in p+p and d+Au collisions at $\sqrt{s_{\rm NN}}$=200 GeV, for comparison with the centrality-binned Au+Au analysis[64]. Like the heavy-ion case, the three HBT radii in p+p exhibit a characteristic decrease with increasing $k_{\rm t}$ (see Fig. 24), thought for p+p it has been attributed to string and multistring fragmentation in earlier studies.

A somewhat surprising result comes about when dividing the Au+Au and d+Au radii by the p+p radii. The divided trends are roughly flat with $k_{\rm t}$ for all radii that indicating an apparent scaling in the $k_{\rm t}$ dependence of the HBT radii for these three systems. Given that the $k_{\rm t}$ dependence presumably arises in very different ways, these results also are a bit puzzling[26].

2.4.5 Azimuthal angle

HBT studies relative to the reaction plane in non-central collision allow the possibility to compare the expanded system's transverse eccentricity at freeze-out with its initial eccentricity from a nuclear overlap model calculation.

STAR had completed an analysis of the azimuthal dependence of HBT radii relative to the reaction plane at $\sqrt{s_{\rm NN}}$=200 GeV[41]. Azimuthally sensitive HBT was suggested[65, 66] as a probe of how spatial anisotropy evolves in non-central collisions. The reasoning is straightforward: (a) The initial almond-shaped geometry gives rise to anisotropies in pressure gradients, the same gradients responsible for elliptic flow. (b) The pressure gradients drive a preferential expansion in the reaction plane that decreases the spatial anisotropy. (c) HBT provides a measure of the freeze-out source shape,which in principle could change its orientation from out-of-plane to in-plane extended depending on the amount of pressure built up and the expansion time.

STAR results had shown an intuitive centrality dependence of the system's eccentricity at freeze-out (see Fig. 25). Near-central collisions showed final eccentricity consistent with zero. When going from central to peripheral collisions, the final eccentricity increased, reflecting the greater initial eccentricity while retaining some of its initial out-of-plane almond shape. Given the strong evidence for significant pressure build-up in the system from elliptic flow measurements, the results point to short evolution times as the dominant cause for out-of-plane freeze-out shapes.

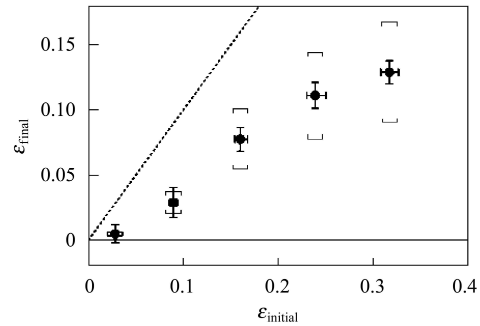

Fig. 25. Source eccentricity obtained with azimuthally sensitive HBT ($\varepsilon_{\rm final}$) vs initial eccentricity from a Glauber model ($\varepsilon_{\rm initial}$). The most peripheral collisions correspond to the largest eccentricity. The dash line indicates $\varepsilon_{\rm initial}=\varepsilon_{\rm final}$. Uncertainties on the precise nature of space-momentum correlations lead to 30% systematic errors on $\varepsilon_{\rm final}$.

2.5 Forward backward multiplicity correlation

The study of correlations among particles production in different rapidity regions may provide understanding of the mechanisms of particle production. Forward-backward multiplicity correlations have been measured in several experiments, mainly in hadron-hadron collisions, to study short and long range correlations[67—73]. The correlation strength is defined by the dependence of the average charged particle multiplicity in the backward hemisphere $\langle N_{\rm b}\rangle$, on the event multiplicity in the forward hemisphere $N_{\rm f}$, $\langle N_{\rm b}\rangle = a+bN_{\rm f}$, where a is a constant and b measures the strength of the correlation[74, 75]:

$$b=\frac{\langle N_{\rm f}N_{\rm b}\rangle-\langle N_{\rm f}\rangle\langle N_{\rm b}\rangle}{\langle N_{\rm f}^2\rangle-\langle N_{\rm f}\rangle^2}=\frac{D_{\rm bf}^2}{D_{\rm ff}^2}$$

$D_{\rm bf}^2$ and $D_{\rm ff}^2$ are the backward-forward and forward-forward dispersions respectively. The correlation strength has the contribution both from short and long range sources. The short range correlation comes from mainly from sources such as resonance decay, cluster formation and jets. The long range part can be obtained by giving a large gap in rapidity between the forward and backward hemisphere.

Figure 26 shows the centrality dependence of backward-forward and forward-forward dispersions measured in Au+Au collisions at $\sqrt{s_{\rm NN}}$=200 GeV[76] $(0.8<|\eta|<1.0)$.

The STAR Collaboration gave the first work on the measurement of the long-range correlation strength (b), in ultra relativistic nucleus-nucleus collisions[77].

The centrality of the collision plays an important role in the growth of long range component of the total correlation strength. Data from 10%—20%, 20%—30%, and 30%—40% most central Au+Au collisions have been analyzed, following the same procedure as for 0%—10% centrality, to determine the evolution of the LRC strength.

Figure 27(a) shows the total correlation strength b. The LRC is shown in Fig. 27(b). The magnitude of the LRC is quite large for the most central collisions when $\Delta\eta > 1.0$. From Fig. 28(b) it is clear that the magnitude of the LRC increases from peripheral to central collisions. The SRC portion of the correlation strength is shown in Fig. 28(a) for mid-central bins.

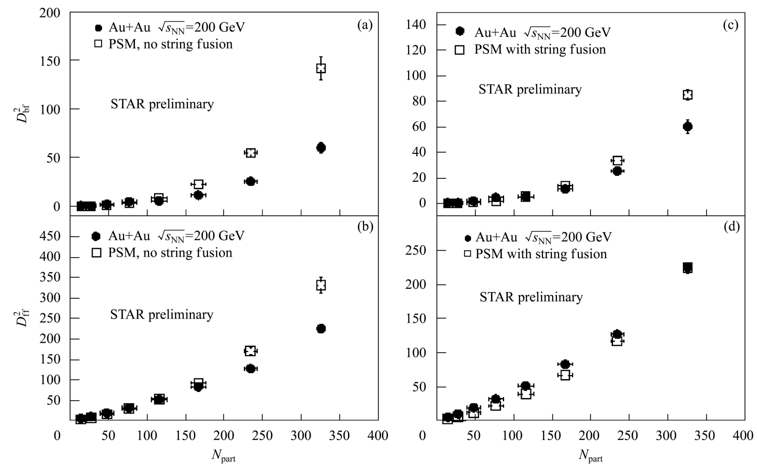

Fig. 26. D^2_{bf}, D^2_{ff} as a function of centrality for Au+Au collision at $\sqrt{s_{NN}}$=200 GeV. Data are compared with PSM calculations with and without string fusion.

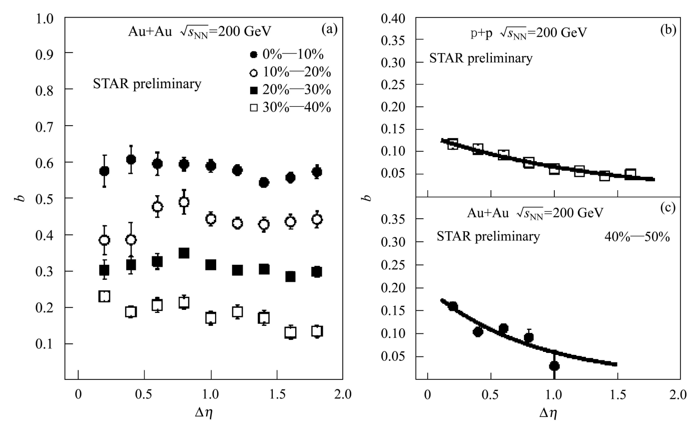

Fig. 27. Correlation strength b as a function of $\Delta\eta$. (a) for Au+Au at four centrality bins; (b) for p+p; (c) for 40%—50% Au+Au.

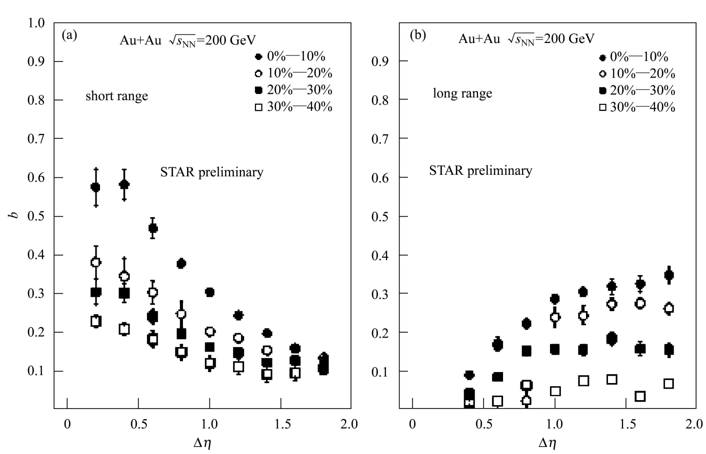

Fig. 28. (a) Short range correlation strength obtained from the scaled b from p+p as a function of pseudorapidity gap; (b) Growth of long range correlation for mid central Au+Au events.

2.6 Fluctuations of elliptic flow

Recently v_2 fluctuation was measured by PHOBOS[78—81] and STAR collaborations[82]. Elliptic flow (v_2) is one of the key observables in understanding the dynamics of heavy ion collisions. The observation of a significant azimuthal anisotropy in the momentum and/or spatial distributions of the detected particles relative to the reaction plane, is direct evidence of interactions between the initially produced particles in heavy ion collisions. These interactions must occur at relatively early time, since expansion of the source rapidly reduces the magnitude of the spatial asymmetry.

Typically, the connection between the initial and final-state anisotropy is provided by hydrodynamical models that related a given, initial source shape to the distribution of produced particles. In such calculation, it is common to use smooth, event-averaged, initial conditions. However, event-by-event fluctuations in the shape of initial interaction region must not be neglected. As a means to quantify the effect of initial-state eccentricity fluctuation, PHOBOS has introduced the "participant eccentricity"[83, 84]. The magnitude and shape of $\epsilon_{\rm part}$ as a function of centrality were found to be robust to variations of the Glauber parameters.

Figure 29 shows first results on event-by-event elliptic flow fluctuations in Au+Au collisions at $\sqrt{s_{\rm NN}}$=200 GeV obtained with the PHOBOS detector.

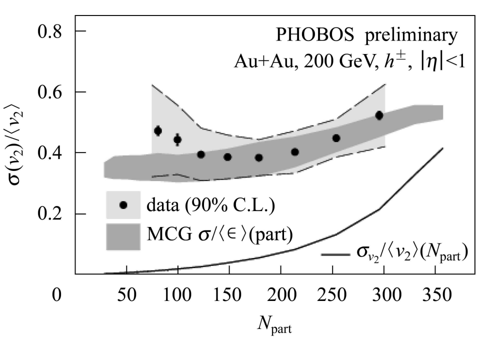

Fig. 29. Relative flow fluctuations, $\sigma_{v_2}/\langle v_2\rangle$, as a function of centrality, for $\sqrt{s_{\rm NN}}$=200 GeV collisions at mid-rapidity, compared with the prediction, $\sigma_\epsilon/\langle\epsilon\rangle$, form the participant eccentricity, and to an estimate of $N_{\rm part}$ induced fluctuations using a fit of $\langle v_2\rangle(N_{\rm part})$.

The participant eccentricity picture accounts for nucleon-position fluctuations in the participating nucleon distributions by calculating the eccentricity, event-by-event, with respect to the principal axes of the overlap ellipse in a MC Glauber (MCG) simulation. In a hydrodynamical scenario, such fluctuations in the shape of the initial collision region would lead naturally to the corresponding fluctuations in the elliptic flow signal. To estimate their magnitude, it is assumed that $v_2 \propto \epsilon$ event-by-event. This leads to $\sigma_{v_2}/\langle v_2\rangle = \sigma_\epsilon/\langle\epsilon\rangle$, where $\sigma_{v_2}(\sigma_\epsilon)$ is the standard deviation of the event-by-event distribution $v_2(\epsilon)$, provided there are no other sources of elliptic flow fluctuations.

2.7 Jet-medium interaction

Jets are produced early, by hard parton-parton scatterings. The scattered partons traverse the dense medium being created in heavy-ion collisions. They are coupled to the medium via strong interactions, lose energy, and fragment into hadrons, likely inside the medium. The fragment hadrons are predominantly soft, but possess characteristic jet-like angular correlations. The degree of energy loss and the changes in jet-like correlations depend on, and thus provide information on the gluon density of the medium[85]. The STAR detector with large acceptance, full azimuth coverage is ideal for jet correlation measurements[86].

2.7.1 Soft-soft correlations

STAR measured the angular correlations between two $p_\perp$ particles without coincidence requirement with a high $p_\perp$ particle. Fig. 30 shows the angular correlations in 130 GeV Au+Au collisions between two soft particles of $0.15<p_\perp<2$ GeV/c[87]. The first and second harmonic terms have been subtracted. The small-angle correlation peak, characteristic of (mini-) jets, narrows in ϕ with centrality, and more dramatically, broadens in η by a factor of 2.3 from peripheral to central collisions[87]. The results demonstrate the strong coupling between these correlated particles and the medium.

2.7.2 Hard-soft correlations

Jets can be more cleanly selected by triggering on high $p_{\rm t}$ particles; A high $p_{\rm t}$ particle likely selects dijets from hard parton-parton scatterings. The hard-scattered partons lose energy in the medium, emerging as lower $p_\perp$ particles than expected from fragmentation in vacuum. Due to energy loss, the measured high $p_\perp$ particles come preferentially from jets produced on the surface of the collision zone and directed outward. The partner jet, directed inward, suffers maximal energy loss resulting in the observed depletion of high $p_\perp$ particles and enhancement of low $p_\perp$ particles[88, 89]. The low $p_\perp$ particles are broadly distributed and appear not much harder than the inclusive hadrons from medium decay[89]. This illustrates that experimentally, the thermalization processes in heavy ion collisions: particle from two distinctively different sources, jets and medium, approaching equilibration via parton-parton interactions.

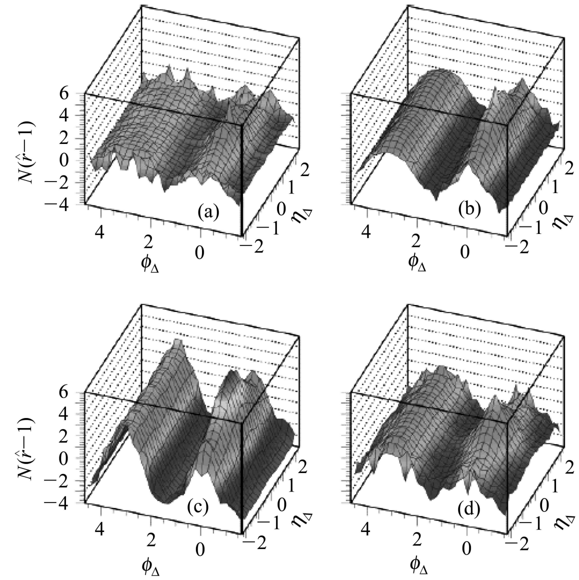

Fig. 30. Angular correlations between soft particle pair of $0.15 < p_\perp < 2$ GeV/c for (a) central to (d) peripheral collisions[87]. The η_Δ independent first and second harmonic terms in ϕ_Δ have been subtracted.

STAR has further studied the azimuthal dependence of associated $\langle p_\perp \rangle$. Fig. 31 shows the number and $p_\perp$-weighted correlation functions in pp, d+Au, and Au+Au collisions[86]. The subtracted background is obtained from mixed-events, modulated by elliptic flow and normalized to the signal in the $0.8 < |\Delta\phi| < 1.2$ region, and is the major source of systematic uncertainties. The pp and d+Au data are similar, and the Au+Au correlation is significantly broader.

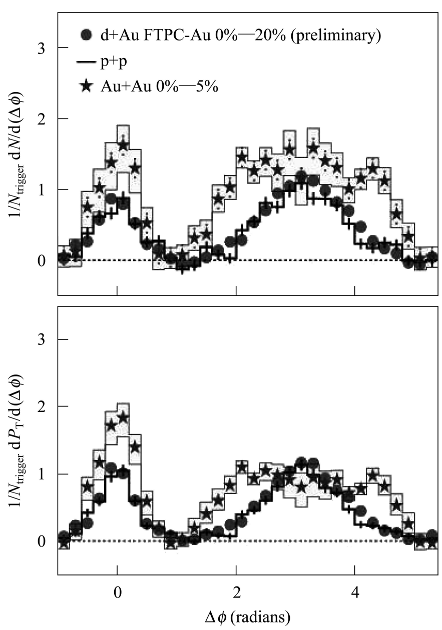

Fig. 31. Background subtracted number (upper) and $p_\perp$-weighted (lower) correlation function in p+p, central 20% d+Au and 5% Au+Au collisions.

Figure 32 shows the $\langle p_\perp \rangle$, obtained from the ratio of the correlation function, as a function of $\Delta\phi$ on the away side. The inclusive hadron $\langle p_\perp \rangle$ is shown as straight line. The $\langle p_\perp \rangle$ for pp and d+Au are peaked at $\Delta\phi = \pi$, as expected from jet fragmentation, and are much larger than the inclusive ones. For central Au+Au collisions, however, the $\langle p_\perp \rangle$ is the smallest at $\Delta\phi = \pi$ for two low trigger $p_\perp$ selections, and appears to be equal to the inclusive $\langle p_\perp \rangle$, while at other angles it is between the values for the simpler systems (p+p and d+Au) and the inclusive data.

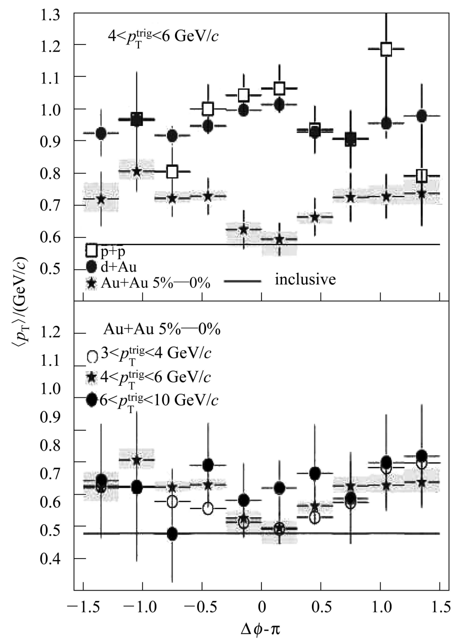

Fig. 32. The $\langle p_\perp \rangle$ of associated hadrons on the away side for the three systems (upper) and three trigger $p_\perp$ selections (lower). The shaded areas are systematic uncertainties.

2.7.3 Three-particle correlations

Two-particle correlations have shown the modification to the away-side shape in central Au+Au collisions relative to p+p, d+Au and peripheral Au+Au collisions. Different scenarios can explain this modification including: large angle gluon radiation, jets deflected by transverse flow, path length dependent energy loss, Cerenkov gluon radiation of fast moving particles, and conical flow generated by hydrodynamic Mach-cone shock-waves. Three-particle correlations have the power to distinguish the scenarios with conical emission, conical flow and Cerenkov radiation, from other scenarios. In addition, the dependence of the observed shapes on the p_t of the associated particles can be used to distinguish conical emission from a sonic boom (Mach-cone) and from QCD-Čerenkov radiation. Very recently, The STAR Collaboration has measured 3-particle azimuthal correlations for a high p_t trigger particle with two softer particles[90, 91]. Results are shown for pp, d+Au and high statistics Au+Au collisions at $\sqrt{s_{\rm NN}}$=200 GeV. An important aspect of the analysis is the subtraction of combinatorial backgrounds, see Fig. 33.

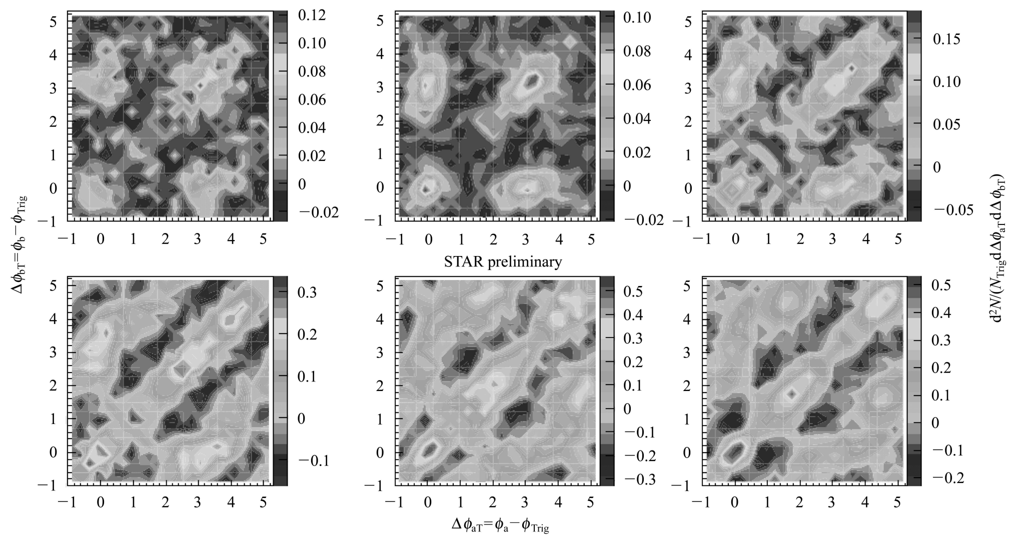

Fig. 33. Background subtracted jet-like 3-particle correlations for p+p (top left), d+Au (top middle), and Au+Au 50%—80% (top right), 30%—50% (bottom left), 10%—30% (bottom center), and ZDC triggered 0%—12% (bottom right) collisions at $\sqrt{s_{\rm NN}}$=200 GeV/c.

The pp and d+Au results are similar with peaks clearly visible for the near-side, (0,0), away-side, (π,π), and the two cases of one particle on the near-side and the other on the away-side, $(0,\pi)$ and $(\pi,0)$. The away-side peak displays on-diagonal elongation is present in the Au+Au results, possibly due to the deflected jets or large angle gluon radiation. The more central Au+Au collisions display an off-diagonal structure, at about $\pi\pm1.45$ radians, that is consistent with conical emission. This structure increases in magnitude with centrality and is prominent in the high statistics top 12% data provided by the online zero degree calorimeter (ZDC) trigger.

3 Outlook

The construction of the LHC machine and the part of the ALICE detector are well under way. ALICE is now in a challenging period in which all the detectors have to be completed, tested and placed in their final position in the ALICE cavern. A detailed installation and commissioning plan, endorsed by the LHC Committee, has been established so that ALICE will be complete and ready in time to measure the first p+p collisions in November 2007. Many physics working groups are preparing and testing the software tools which will permit to analyze the huge quantity of expected data using the GRID technologies.

LHC will explore new aspects of the strongly-interacting matter. Many of them will be investigated by the so called "soft" probes. The characteristics of the ALICE detector (i.e. particle identification, low $p_{\rm t}$ cut-off, excellent tracking and vertexing capability) will permit to study the nature of the bulk, its collective behavior and the influence of the hard process on its properties.

References

1 WANG Ya-Ping et al. Chin. Phys. C (HEP & NP), 2008, **32**(4): 308

2 WANG Ya-Ping, ZHOU Dai-Mei, CAI Xu. Collective Expansion and Hadronization in High Energy Heavy Ion Colliaion Experiments. Accepted by Chin. Phys. C (HEP & NP)

3 CAI Xu, ZHOU Dai-Mei. HEP & NP, 2002, **26**(9): 971—990 (in Chinese)

4 Heiselberg H. Physics Report, 2001, **351**: 161—194

5 Stephanov M, Majagopal K, Shuryak E. Phys. Rev. D, 1999, **60**: 114028

6 Lungwitz B et al. (NA49 Collaboration). nucl-ex/0610046

7 CHAI Z W et al. (PHOBOS Collaboration). J. Phys. Conf. Ser., 2005, **27**: 128

8 Wozniak K (PHOBOS Collaboration). J. Phys. G: Nucl. Part. Phys., 2004, **30**: S1377—S1380

9 Afanasiev S V et al. (NA49 Collaboration). Phys. Rev. Lett., 2001, **86**: 1965—1969

10 Das S et al. (STAR Collabration). nucl-ex/0503023

11 Voloshin S A, Koch V, Ritter H G. Phys. Rev. C, 1999, **60**: 024901

12 Adcox K et al. (PHENIX Collabration). Phys. Rev. C, 2002, **66**: 024901

13 Adler S S et al. (PHENIX Collabration). Phys. Rev. Lett., 2004, **93**: 092301

14 Adams J et al. (STAR Collaboration). Phys. Rev. C, 2005, **72**: 044902

15 Gazdzicki M, Mrowczynski S. Z. Phys. C, 1992, **54**: 127

16 Adams J et al. (STAR Collaboration). Phys. Rev. C, 2005, **71**: 064906
17 Adams J et al. (STAR Collaboration). J. Phys. G, 2006, **32**: L37—L48
18 LIU Q J, Prindle D J, Trainor T A. Phys. Lett. B, 2006, **632**: 197—202
19 Pearson K. Phil. Trans. Royal Soc., 1896, **187**: 253
20 Trainor T A. hep-ph/0001148
21 Appelshauser H et al. (NA49 Collaboration). Phys. Lett. B, 1999, **459**: 679—686
22 Adamova D et al. (CERES Collaboration). Nucl. Phys. A, 2003, **727**: 97—119
23 Adams J et al. (STAR Collaboration). J. Phys. G, 2007, **33**: 451—466
24 Quantity $\nu \approx 2N_{\rm bin}/N_{\rm part}$, where $N_{\rm bin}$ is the average number of N-N collisions experienced by a participant nucleon and $N_{\rm part}$ is the average participant nucleon number,estimates the mean participant path length in number of encountered nucleons
25 Heinz U, Jacak B V. Ann. Rev. Nucl. Part. Sci., 1999, **49**: 529
26 Dan Magestro. J. Phys. G, 2005, **31**: 265—272
27 Adamova D et al. (CERES Collaboration). Nucl. Phys. A, 2003, **714**: 124—144
28 Lisa M A et al. (E895 Collaboration). Phys. Rev. Lett., 2000, **84**: 2798—2802
29 Adler C et al. (STAR Collaboration). Phys. Rev. Lett., 2001, **87**: 082301
30 Bearden I G et al. (NA44 Collaboration). Phys. Rev. C, 1998, **58**: 1656—1665
31 Aggarwal M M et al. (WA98 Collaboration). Eur. Phys. J. C, 2000, **16**: 445—454
32 Soltz R et al. (E866 Collaboration). Nucl. Phys. A, 1999, **661**: 439c—443c
33 Kolb P F, Heinz U. nucl-th/0305084
34 Heinz U, Kolb P F. Nucl. Phys. A, 2002, **702**: 269—280
35 Ahle L et al. (E802 Collaboration). Phys. Rev. C, 2002, **66**: 054906
36 Appelshauser H et al. (NA49 Collaboration), Eur. Phys. J. C, 1998, **2**: 661—670
37 Aggarwal M M et al. (WA98 Collaboration). Phys. Rev. C, 2003, **67**: 014906
38 Antinori F et al. (WA97 Collaboration). J. Phys. G, 2001, **27**: 2325—2344
39 Adamova D et al. (CERES Collaboration). Nucl. Phys. A, 2003, **714**: 124—144
40 Adcox K et al. (PHENIX Collaboration). Phys. Rev. Lett., 2002, **88**: 192302
41 Adams J et al. (STAR Collaboration). Phys. Rev. Lett., 2004, **93**: 012301
42 Adams J et al. (STAR Collaboration). Phys. Rev. C, 2005, **71**: 044906
43 Adler S S et al. (PHENIX Collaboration). Phys. Rev. Lett., 2004, **93**: 152302
44 Lisa M A et al, Ann. Rev. Nucl. Part. Sci., 2005, **55**: 357—402. nucl-ex/0505014
45 Gyulassy M, Padula S S. Phys. Rev. C, 1990, **41**: R21
46 Schnetzer S et al. Phys. Rev. Lett., 1982, **49**: 989—992
47 Akiba Y et al. (E-802 Collaboration). Phys. Rev. Lett., 1993, **70**: 1057—1060
48 Beker H et al. (NA44). Z. Phys. C, 1994, **64**: 209—217
49 Cianciolo V. Nucl. Phys. A, 1995, **590**: 459—464
50 Miskowiec D et al. Nucl. Phys. A, 1996, **610**: 227—239
51 Akkelin S V, Sinyukov Y M. Phys. Lett. B, 1995, **356**: 525—530
52 Csorgo T, Lorstad B. Phys. Rev. C, 1996, **54**: 1390—1403
53 Wiedemann U A et al. Phys. Rev. C, 1996, **53**: 918—931
54 Wiedemann U A, Heinz U W. Phys. Rep., 1999, **319**: 145
55 Beker H et al. (NA44 Collaboration). Phys. Rev. Lett., 1995, **74**: 3340—3343
56 Bearden I G et al. (NA44 Collaboration). Phys. Rev. Lett., 2001, **87**:112301
57 Ahle L et al. (E-802 Collaboration). Phys. Rev. C, 2002, **66**: 054906
58 Afanasiev S V et al. (NA49 Collaboration). Phys. Lett. B, 2003, **557**: 157—166
59 Appelshauser H et al. (NA49 Collaboration). Phys. Lett. B, 1999, **467**: 21—28
60 Aggarwal M M et al. (WA98 Collaboration). Phys. Rev. Lett., 2004, **93**: 022301
61 Heffiner M (PHENIX Collaboration). J. Phys. G, 2004, **30**: S1043—S1047
62 Bekele S (STAR Collaboration). J. Phys. G, 2004, **30**: S229—S234
63 Renault G (STAR Collaboration). hep-ex/0404024
64 Thomas D Gutierrez (STAR Collaboration). nucl-ex/0403012
65 Voloshin S A, Cleland W E. Phys. Rev. C, 1996, **53**: 896
66 Wiedemann U A. Phys. Rev. C, 1998, **57**: 266—279
67 Uhlig S et al. Nucl. Phys. B, 1978, **132**: 15—28
68 Alner G J et al. Phys. Rep., 1987, **154**: 247—383
69 Ansorge R E et al. Z. Phys. C, 1988, **37**: 191
70 Alexopoulos T et al. Phys. Lett. B, 1995, **353**: 155—160
71 Derado I et al. Z. Phys. C, 1988, **40**: 25—27
72 Bachler J et al. (NA35 Collaboration). Z. Phys. C, 1992, **56**: 347
73 Akiba Y et al. (E-802 Collaboration). Phys. Rev. C, 1997, **56**: 1544—1552
74 Capella A, Krzywicki A. Phys. Rev. D, 1978, **184**: 120
75 Capella A et al. Phys. Rep., 1994, **236**: 225—329
76 Tarnowsky T J (STAR Collaboration). nucl-ex/0606018
77 Srivastava B K (STAR Collaboration). nucl-ex/0702054
78 Loizides C et al. (PHOBOS Collaboration). nucl-ex/0611017
79 Loizides C et al. (PHOBOS Collaboration). nucl-ex/0701049
80 Manly S et al. (PHOBOS Collaboration). nucl-ex/0702029
81 Alver B et al. (PHOBOS Collaboration). nucl-ex/0702036
82 Sorensen P et al. (STAR Collaboration). nucl-ex/0612021
83 Manly S et al. (PHOBOS Collaboration). Nucl. Phys. A, 2006, **774**: 523—526
84 Alver B et al. (PHOBOS Collaboration). nucl-ex/0610037
85 WANG X N, Gyulassy M. Phys. Rev. Lett., 1992, **68**: 1480—1483
86 WANG Fu-Qiang et al. (STAR Collaboration). J. Phys. Conf. Ser., 2005, **27**: 32—41
87 Adams J et al. (STAR Collaboration). Phys. Rev. C, 2006, **73**: 064907
88 Adler C et al. (STAR Collaboration). Phys. Rev. Lett., 2003, **90**: 082302
89 Adams J et al. (STAR Collaboration). nucl-ex/0501016; WANG F (STAR Collaboration). J. Phys., 2004, **30**: S1299
90 Ulery J G et al. (STAR Collaboration). nucl-th/07040220
91 Ulery J G et al. (STAR Collaboration). nucl-th/07040224